Preprint Cambridge Centre for Computational Chemical Engineering ISSN 1473 – 4273

Temperature and CH* Measurements and Simulations of Laminar Premixed Ethylene Jet-Wall Stagnation Flames

Jochen A.H. Dreyer[1,2], Eric J. Bringley[1], Manoel Y. Manuputty[1,2], Jethro Akroyd[1,2], Markus Kraft[1,2,3]

released: November 1, 2019

[1] Department of Chemical Engineering and Biotechnology
University of Cambridge
Philippa Fawcett Drive
Cambridge, CB3 0AS
United Kingdom

E-mail: mk306@cam.ac.uk

[2] CARES
Cambridge Centre for Advanced Research and Education in Singapore
1 Create Way
CREATE Tower, #05-05
Singapore, 138602

[3] School of Chemical and Biomedical Engineering
Nanyang Technological University
62 Nanyang Drive
Singapore, 637459

[4] CoaST
Department of Chemical and Biochemical Engineering
Technical University of Denmark (DTU)
Building 229
2800 Kgs. Lyngby
Denmark

Preprint No. 250

Keywords: thin film pyrometry, optical CH* measurements, stagnation flames, 1D simulation, 2D simulation

Edited by
Computational Modelling Group
Department of Chemical Engineering and Biotechnology
University of Cambridge
Philippa Fawcett Drive
Cambridge CB3 0AS
United Kingdom

E-Mail: c4e@cam.ac.uk
World Wide Web: http://como.ceb.cam.ac.uk/

Abstract

New experimental 2D measurements are reported to characterise the flame location, shape and temperature of laminar premixed ethylene jet-wall stagnation flames when the equivalence ratio, exit gas velocity and burner-plate separation distance are varied. Bandpass-filtered optical measurements of the CH* chemiluminescence were used to provide information about the shape and location of the flames. Thin filament pyrometry (TFP) using a 14 μm diameter SiC filament was used to make line measurements of the temperature to reconstruct the full 2D temperature field for the first time in premixed, jet-wall stagnation flames. The comparison of CH* measurements with (intrusive) and without (non-intrusive) the presence of the SiC filament showed that the filament resulted in minimal disturbance of the flame when the filament was placed downstream of the flame front. However, the flame was observed to attach to the filament, resulting in more significant disturbance, when the filament was placed upstream of the flame front. The flames were simulated using both 1D and 2D models. The 2D simulations were used to provide estimates of the velocity, kinematic viscosity and thermal conductivity required to obtain the gas temperature from the TFP data. The 1D simulations showed excellent agreement with the experimentally observed centreline quantities, but required the strain boundary condition to be fitted in order to match the experimentally observed flame location. The 2D simulations showed excellent agreement without the need for any fitting, and correctly predicted the flame shape, location and temperature as the experimental conditions were varied. A comparison of the set of simulated temperature-residence time distributions showed relatively uniform distributions within each flame. However, the most uniform set of distributions did not correlate with the flattest flame.

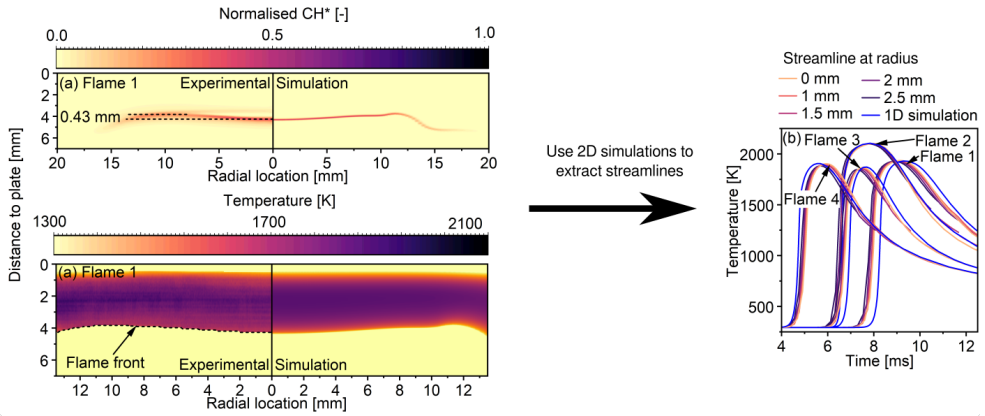

Highlights

- New measurements of CH* and temperature are reported as 2D fields.
- Temperature measurements using SiC filaments create minimal disturbance.
- 1D simulations give good temperature profiles but rely on prior experiments.
- 2D simulations predict the observed changes in shape and temperature.
- Temperature-residence time distributions were approximately uniform.
- The most uniform set of distributions did not come from the flattest flame.

Contents

1 Introduction

Laminar flames are widely used as a tool to study the physics and chemistry of combustion systems, including the processes responsible for the formation of combustion generated particles [11]. One type of laminar flame that has gained recent interest in both fundamental combustion research [4, 43] as well as material synthesis applications [26, 38] are premixed, jet-wall stagnation flames.

One advantage of premixed, jet-wall stagnation flames is that the stagnation plane is well defined; the heat loss to the stagnation surface has been shown to have little effect on the reactions at the flame front [14]. This makes them particularly useful for studying laminar flame speeds [21, 39]. Stagnation flames have been proposed as a source of data for the optimisation of chemical mechanisms. Centreline velocity and CH* profiles for C_1 and C_2 flames were initially published [4, 7] followed by C_3 and C_4 alkanes and C_1- C_4 alcohols with added data of NO profiles [42, 43]. This data was used to optimise NO [42] and CH [40] reaction rates.

Premixed stagnation flames are "approximately flat" and axially symmetric, thus facilitating modelling efforts. The most widely used approach to simulate such flames is to use a 1D model based on the stream function assumption [20]. This approach is computationally efficient, but is limited to idealised flows with constant radial pressure gradients and radially uniform profiles [5, 9, 15, 29]. An alternate approach is to solve the full set of Navier-Stokes and conservation equations for chemically reacting flow, while making use of symmetry to reduce the problem from 3D to 2D.

The applicability of 1D models has been the subject of many studies for counterflow [19, 29] and jet-wall stagnation flames [7, 9, 36]. Discrepancies between 1D and 2D models have largely been attributed to differences in the non-uniform pressure curvature [9, 29, 36]. Bergthorson and coworkers [4–6] have shown that the assumptions made in the 1D model are satisfied if the boundary conditions are specified appropriately after the free-jet region. Bouvet et al. [9] studied a confined, jet-wall stagnation flame and also found the 1D simulation was unable to simulate the free-jet due to the non-uniform pressure curvature. Johnson et al. [19] showed that the 1D approach is applicable for counterflow streams from contoured nozzles of greater than 13 mm diameter because of the negligible contribution of radial terms on the momentum and energy equations.

Most applications of 2D simulations have focused on either coflow diffusion flames [35] or non-premixed counterflow flames [32]. Only a few works have considered 2D simulations of premixed, jet-wall flames [9, 36]. Sone [36] performed 2D simulations of premixed stagnation flames but focused on analysis of centreline profiles, making only one comparison against 2D CH planar laser induced fluorescence data. With the exception of velocity profiles [1, 9], very few works compare 2D simulations of premixed, jet-wall stagnation flames to 2D experimental data. Such comparisons would be useful when using premixed, jet-wall flames for material synthesis applications.

The purpose of this paper is to experimentally characterise and model premixed, jet-wall stagnation flames in two dimensions. The flame position, shape, and temperature are measured experimentally as 2D fields. To the best of our knowledge, this is the first application of thin filament pyrometry to jet-wall stagnation flames. The extent of the

disturbance of the flame due to the temperature measurements is assessed. It is evaluated whether 1D and 2D models can reproduce the experimental observations when the nozzle-stagnation surface distance, burner exit velocity and ethylene-air equivalence ratio are varied. Information from the 2D simulations is extracted along streamlines and compared to assess the uniformity of the temperature-residence times.

2 Experimental

2.1 Premixed Stagnation Flame Apparatus

An in-house built burner was used to study premixed jet-wall stagnation flames on a water-cooled stagnation surface. The ethylene/air mixture is introduced at the bottom of the burner, homogenised through glass beads and a pourous plug, and accelerated in a contoured nozzle to create a plug flow velocity profile at the exit (diamter $d = 14$ mm). Nitrogen is used as a sheath gas to shield the flame from ambient air. A thermocouple is flush with the stagnation plate and measures the temperature at the stagnation point, T_{stag}. A figure of the burner can be found in the supporting information (Fig. 6).

Four flame conditions, summarised in Table 1, were studied. All of the gas flows were controlled with Bronkhorst mass flow controllers. The nitrogen flow rate was set such that the flow velocity was 150 cm s^{-1} for all experiments. The other conditions were chosen to study the effect of flow velocity at the nozzle exit v, equivalence ratio ϕ, and ratio between the nozzle-stagnation plate distance L to nozzle diameter d.

2.2 CH* Chemiluminescence Measurements

The chemiluminescence of CH* was recorded with a Blackfly S camera equipped with a MVL25M23 lens from Thorlabs with an aperture set to f/1.4 and a focal length of 25 mm. A 430 nm bandpass filter (Thorlabs, FWHM 10 nm) was used to image the light emitted during the $A^2\Delta \rightarrow X^2\Pi$ relaxation of the thermally excited CH radicals. The 2D

Table 1: *Flame conditions for the four flames studied. ϕ is the equivalence ratio, v is the burner exit velocity, L/d is the ratio between the burner-surface separation to nozzle diameter, T_{stag} is the measured temperature of the stagnation surface and a_{1D} is the strain used for the boundary conditions to the 1D model. The nitrogen flow velocity was 150 cm s^{-1} for all experiments.*

Flame	ϕ -	v cm s^{-1}	L/d -	a_{1D} s^{-1}	T_{stag} K
1	0.7	200	1	27.5	497
2	0.8	200	1	46.5	522
3	0.7	300	1	22.0	524
4	0.7	200	0.6	163.3	513

projection recorded by the camera was transformed into a 2D cross section by making use of the flame symmetry and applying an inverse Abel transform using the basis-set expansion (BASEX) method [2, 13]. All results were normalised by the highest CH* emission recorded, which was the peak emission from Flame 2 in this study.

2.3 Thin Filament Pyrometry

The flame temperatures were measured using SiC thin filament pyrometry (TFP) [22]. The light emission from a SiC filament placed into the flame is used to infer the temperature of the surrounding gas. The approach applied here infers the filament temperature, T_{SiC}, by comparing the ratio of observed intensities of colour channels to a previously generated temperature look-up table [25]. Three replicate measurements were taken of each flame. T_{SiC} was converted to gas temperature using an energy balance of radition and forced convection over an inclined cylinder. The equations, S-type thermocouple calibration procedure, and further details regarding the calculation of the temperature look-up table are fully described in literature [12, 22, 24]. Additional details regarding this method, the image processing, and the equipment used can be found in the supporting information (A).

3 Simulations

The chemical mechanism used in the 1D and 2D models in this study was the San Diego Mechanism [46] because of its past success in modelling ethylene stagnation flames [3, 4, 7]. Full coupling of sub-mechanisms for CH* were previously shown to have negligible effects on the flame characteristics due to its orders of magnitude difference in concentration [31, 41]. Therefore, CH* species profiles are calculated as a post-process assuming it is in quasi-steady state. Production of CH* from C_2H and O or O_2 and quenching from spontaneous emission (described by the Einstein coefficient) and reactions with H_2O, CO_2, CO, H_2, O_2, CH_4, and N_2 were considered; all rates and Einstein coefficients can be found in Table 2.2 in [31].

3.1 1D Simulations

The stagnation flame is described by 1D ordinary differential equations when an axisymmetric streamfunction assumption is applied to the full governing equations [20]. The model equations are fully documented in previous work [23, 27]. The calculations were performed using *k*inetics® software package [10]. The simulated domain extends between the nozzle outlet and the stagnation plate. A rigorous approach to define the boundary conditions would require velocimetry measurements to fully characterise the flow field [4, 7]. In the absence of such measurements, the strain rate at the burner exit was varied such that the location of the CH* peak matched experimental observations, similar to the approach used in previous work [23]. The values of the final strain rates used are reported in Table 1.

3.2 2D Simulations

The finite volume method was used to discretise the governing equations into algebraic equations in a 2D axisymmetric space. OpenFOAM [37] was used to solve the discretised equations using the transient PISO Algorithm [18]. The *k*inetics® Application Programming Interface [10] was used to calculate detailed transport coefficients and chemical source terms guaranteeing consistency between the two sets of simulations. The simulated domain starts upstream of the nozzle inside the burner and extends radially outward from the burner to capture the full flow field over the stagnation plate. A mass flux boundary conditions was specified to match the experimental conditions upstream of the nozzle. Isothermal and no-slip conditions specified at walls and ambient pressure outlets at the radial simulation boundary. A figure showing the computational domain can be found in Fig. 7 of the supporting information.

4 Results and Discussion

4.1 Flame Position and Shape

The flame positions and shapes from the 2D simulations and experiments were assessed by comparing the normalised 2D profiles of CH* (Fig. 1). The chemiluminescence was noninvasively measured and can be compared without concerns about flame disturbance. Overall, the agreement between the simulations and experiments is very good. All of the flame positions and major trends with changing flame parameters are captured by the 2D simulations. Oscillations are observed at the flame edge ($r > 11$ mm) in both simulations and experiments (Fig. 1), but repeated experimental measurements leads to time averaged results. Because the oscillations are outside the region of interest ($r < 11$ mm), instantaneous simulation results are compared to the experimental results.

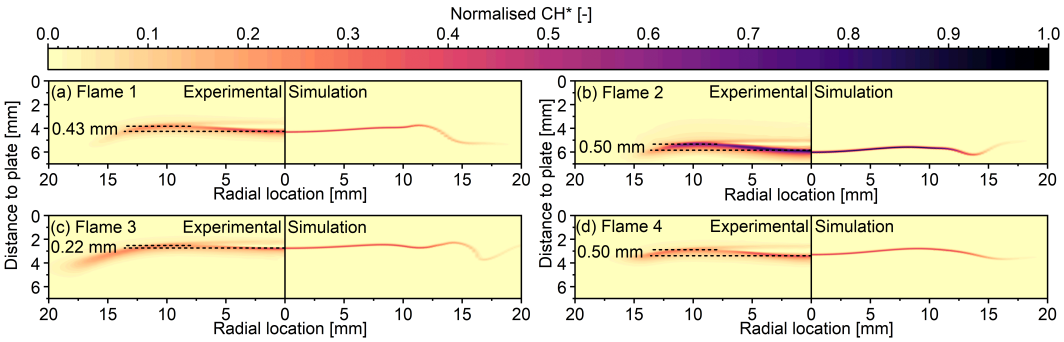

Figure 1: *Normalised CH* profiles obtained from experiments by recording the CH* chemiluminescence (left-hand panes) and the 2D simulations (right-hand panes). The dotted lines mark the points used to calculate the difference in vertical position, ε.*

Flame 1 is located 4.3 mm from the plate, with its centre slightly curved towards the burner nozzle (Fig. 1a). The extent to which the flame was curved was quantified by calculating

the difference between the vertical position of the flame centre and the position where the flame wing was closest to the plate, ε (analogous to the amplitude of a transverse wave, $\varepsilon = 0.43$ mm for Flame 1; see Fig. 1), and by calculating the arc-chord ratio, γ, (1.0178 for Flame 1) over the same region. Increasing the equivalence ratio in the experiments from $\phi = 0.7$ to $\phi = 0.8$ causes the flame to move closer towards the nozzle (5.8 mm from the plate) and to become more curved (Fig. 1b; $\varepsilon = 0.50$ mm; $\gamma = 1.0312$). Simultaneously, the normalised CH* signal more than doubles as seen from the colour scale in Fig. 1 as well as extracted line plots shown in Fig. C2 of the Supporting Information. The simulation predicts a flame location of 6.0 mm, captures the change in shape, and also predicts a twofold increase in CH*. The reason that the flame front shifts towards the burner is that the laminar flame speed is increased when the equivalence ratio is increased from $\phi = 0.7$ to $\phi = 0.8$. The increased CH* amount can be explained by the larger relative concentration of ethylene and the increase in temperature. Flames have been shown to curve as they move closer to the burner because the centreline flow is decelerated due to a build up in stagnation pressure [39].

When the experimental burner exit velocity was increased from 200 cm s^{-1} to 300 cm s^{-1}, the flame moved closer to the plate (2.8 mm) and became less curved (Fig. 1c; $\varepsilon = 0.22$ mm; $\gamma = 1.0093$). This is expected because the cold gas velocity has increased while the laminar flame speed remains unchanged. Similar observations have been made by other researchers [14, 39]. The 2D simulations capture both the shift of the flame towards the stagnation plate (2.8 mm) as well as the flattening of the flame shape.

Moving the burner nozzle closer to the stagnation plate shifts the flame closer to the plate and significantly curves the flame (Fig. 1d; $\varepsilon = 0.50$ mm; $\gamma = 1.0199$). This trend can be seen both, in the experimental as well as simulated CH* profiles. The reason for the more curved flame is that the stagnation pressure propagates into the nozzle for small separation distances [5]. This leads to an increased centreline deceleration and more curved flames [39].

4.2 Flame Disturbance by SiC Filament

Intrusive techniques always pose the risk that they disturb the flame such that the measurements are not representative of the undisturbed flame. To investigate how the filament disturbs the flame, images of the CH* chemiluminescence were taken with and without a filament inside the flame (Fig. 2). It should be noted that Abel inversion was not applied here because rotational symmetry is broken when the filament is present.

Placing the 14 μm SiC filament into the flame has no major effect on the flame shape or position (Fig. 2). In fact, the changes are too small to clearly see them in Fig. 2 but they can be observed when plotting the recorded intensity over the distance to the plate (Fig. 9 in the Supporting Information). The only slight difference between flames with and without the filament can be seen when the filament is positioned upstream of the flame (i.e., in the pre-heat zone of the flame). In such cases, it is noted that the flame attached to the filament and caused the flame to become slightly stretched. This is in agreement with previous studies where thermocouples were used in these type of flames [38]. It can also be observed that the flame disturbance is less when the flow velocity is increased (compare

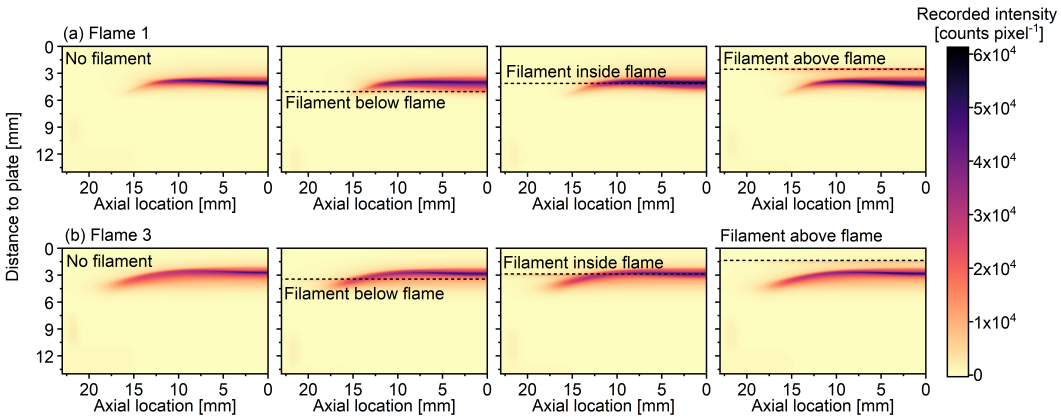

Figure 2: *Recorded CH* chemiluminescence from the undisturbed flames (left-hand panes) and from the flames with a SiC filament inside their centre at different distances from the plate.*

Flame 1 and 3 in Fig. 2). It is also interesting to note that measuring the centre-line temperature directly by positioning the filament vertically into the flame proved impractical due to the significant flame disturbance (Fig. 10 in Supporting Information).

4.3 Flame Temperature Profiles

The 2D temperature profiles and selected line profiles are shown in Fig. 3 and Fig. 4, respectively. Because the flame was shown to attach to the filament when positioned upstream of the flame front (Section 4.2), only temperature downstream of the flame front are shown. For the purpose of these figures, the flame front was defined as the maximum in CH* chemiluminescence recorded from the undisturbed flame. Nevertheless, a slightly higher temperature can be observed in pre-heat zone of the experimental results, most likely due to the flame attachment and accompanied shift in the high-temperature region.

The absolute temperatures and trends with changing flame parameters are in excellent agreement between the experiments and 2D simulations (Fig. 3). Increasing the equivalence ratio from $\phi = 0.7$ to $\phi = 0.8$ increases the flame temperature by about 170 K. The reason is the increase in the adiabatic flame temperature from $T_{ad} = 2001$ K to 2165 K (calculated using *k*inetics® [10]). When the flame was closer to the plate, the heat loss to the water-cooled stagnation surface increases and thus cools the flame slightly ($\sim$60 K from Flame 1 to 3 and $\sim$30 K from Flame 1 to 4). The increased heat loss can also be seen in the increase in the stagnation plate temperature T_{stag} reported in Table 1.

Temperatures obtained from the 1D simulations are also shown in Fig. 4. They are essentially identical to the centre-line temperatures obtained from the 2D simulations. The only noticeable difference is that the onset of the temperature rise is slightly shifted for Flame 2 and 4. The reason for this is that the boundary conditions for the 1D simulations were chosen such that the CH* peak matches the experiments exactly (see Fig. 8) while the 2D simulations predict the flame positions based on the experimental parameters. Thus the 1D simulations require some kind of experimental characterisation of the flame (CH*

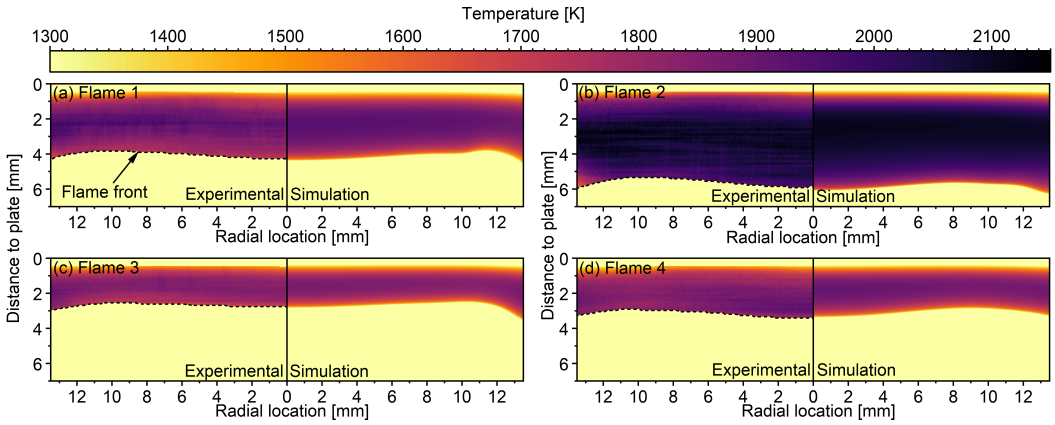

Figure 3: *Cross sections of temperature profiles from thin filament pyrometry experiments (left-hand panes) and 2D simulations (right-hand panes). The average of three repeat measurements are reported.*

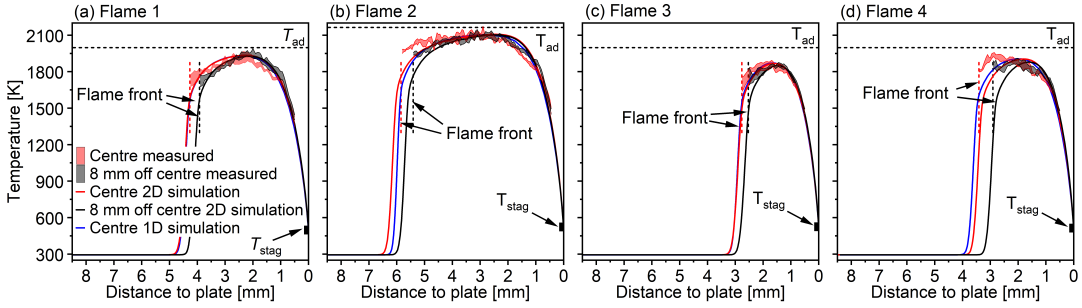

Figure 4: *Extracted temperature profiles along $r = 0$ mm and $r = 8$ mm for experiments and 2D simulation and 1D simulation of centreline values. Three repetitions were measured. The standard deviation of the temperature measurements is shown as shaded area with the average being in its centre.*

profiles as in this study or velocity fields as in [4, 43]) while the 2D simulations are predictive.

4.4 Temperature-Residence Time Profile

The 2D simulations can be used to extract a number of quantities of interest. Given that premixed stagnation flames are increasingly used for nanoparticle synthesis [27, 38], one quantity that might be of particular interest is time-temperature curves along streamlines. These could be used to assess the temperature history nanoparticles experience during synthesis and serve as input to models that resolve the evolution of a population of particles with a given chemical environment[23].

Velocity profiles of Flame 1 superimposed with vector fields and calculated streamlines are shown in Fig. 5a (see Fig. 11 for other flames). The temperatures as function of residence time along these streamlines are plotted in Fig. 5b. The time-temperature curves of the 1D model agree reasonably well with the results at $r = 0$ from the 2D simulations. The

onset in temperature rise seems to be shifted slightly which might be due to the differences in flame positions (see Fig. 8) or the boundary conditions imposed in the 1D model (see Section 4.3). Comparing the streamlines at different radial positions reveals that they do differ slightly for some flames, such as the peak temperatures experienced in Flame 3 and 4. The differences in streamline profiles are consequences of intricately linked reasons, such as a shift in flame front towards the burner close to the axis of symmetry for the highly curved flames. However, even after shifting the profiles such that the pre-heat zone overlaps at all radial positions, a slight spread of the profiles can be observed (Fig. 12). To what extent this influences particle properties during material synthesis will be the subject of a later study. It is interesting to note however that the streamline profiles appear to overlap most for Flame 2 even though it showed the highest tortuosity of all flames (Fig. 1). Thus, optical inspection of the flame shape seems to be insufficient to assess how similar the streamlines at different radial positions will be.

5 Conclusions

The flame location, shape, and temperature was characterised as 2D fields using CH* chemiluminescence and thin filament pyrometry to capture the changes in a premixed, jet-wall stagnation flame when varying the equivalence ratio, exit gas velocity, and burner-plate separation distance. The SiC filament does not disturb the flame when downstream of the flame front but the flame was found to attach when the filament is is placed upstream of the flame front. Information from 2D simulations allow for TFP measurements to infer the gas temperature by performing a heat balance over the filament.

The new experimental data is compared to 1D and 2D simulations. The computed temperature profiles are in excellent agreement with the experimentally observed temperature. However, the 2D simulations only require trivial boundary conditions (such as mass flux) to predict the flame properties while additional full specification of the strain rate boundary condition are required for the 1D simulation. The additional radial information provided by the 2D simulations allows for streamline profiles to be extracted off centreline. The temperature-residence time distributions of each flame was found to be approximately

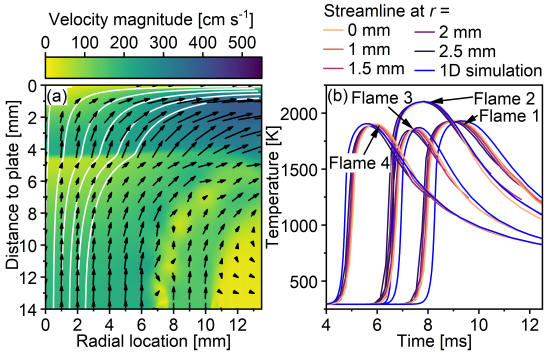

Figure 5: *(a) 2D velocity-streamline plot for Flame 1 and (b) temperature-residence time plot for all flames. The abrupt change in the streamlines occurs at the flame front (left panel).*

uniform, however, the uniformity was not found to correlate with the flatness of the flame.

6 Acknowledgements

This work was partly funded by the National Research Foundation (NRF), Prime Minister's Office, Singapore under its CREATE programme. E.J.B. was funded by a Gates Cambridge Scholarship (OPP1144).

A Experimental Details

A.1 Burner Apparatus

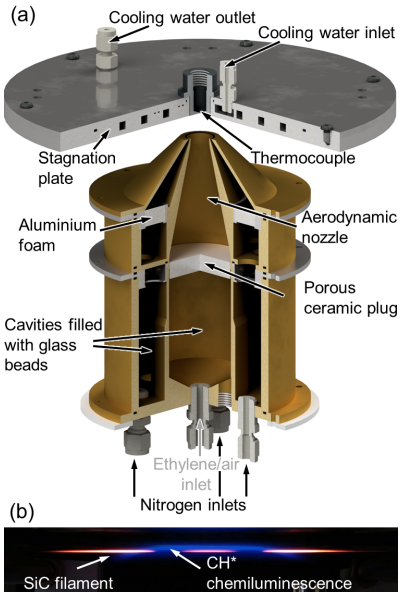

Figure 6: *(a) Rendered CAD drawing of the in-house developed premixed burner and water cooled stagnation surface. (b) Photograph of the SiC filament inside the premixed stagnation stabilised flat flame.*

A burner was used to study premixed hydrocarbon flames stabilised on a water-cooled stagnation surface. An ethylene/air mixture is introduced at the bottom of the burner (Fig. 6a). The premixed gas is expanded in a central cylinder with diameter of 50 mm filled with glass beads to homogenise the flow. The flow then passes through a porous ceramic plug to remove remaining fluctuations, before the gas is accelerated in a contoured nozzle. The inner shape results in a plug flow at the nozzle exit (diameter d = 14 mm) and facilitates the stabilisation of a flat flame.

Nitrogen is used as a sheath gas and is introduced through three ports at the bottom of the burner. It is distributed and stabilised with the aid of glass beads and a porous aluminium foam. The nitrogen is accelerated in a contoured nozzle and exits around the central nozzle to shield the flame from ambient air.

A water cooled, stainless steel plate was used as the stagnation surface. The cooling water enters close to the centre of the plate, flows trough a spiral shaped channel and exits on the outer edge of the plate. A cylindrical plug is placed in the centre of the plate to accommodate a thermocouple. The thermocouple tip is flush with the stagnation plate and measures the temperature at the stagnation point, T_{stag}.

A.2 Thin Filament Pyrometry Details

The SiC filament temperature T_{SiC} was calculated from its colour. The ratio of the colour channels recorded by a camera hereby depend on T_{SiC} and emissivity ε of the imaged material [22, 24, 25]:

$$\frac{R_i}{R_j} = \frac{\int_0^\infty \eta_i(\lambda)\frac{\varepsilon}{\lambda^5}[\exp(hc/\lambda\sigma T_{\mathrm{SiC}})-1]^{-1}\mathrm{d}\lambda}{\int_0^\infty \eta_j(\lambda)\frac{\varepsilon}{\lambda^5}[\exp(hc/\lambda\sigma T_{\mathrm{SiC}})-1]^{-1}\mathrm{d}\lambda}, \tag{A.1}$$

where R_i and η_i are the light intensity and wavelength-dependent camera response of colour channel i, λ is the wavelength, σ is the Boltzmann constant, h is the Planck constant, and c is the speed of light. The shape of the η_i curves was obtained using the quantum efficiency of the camera and wavelength-dependent filter and lens transmission data provided by the respective manufacturers. Following the procedure of Ma and Long[24], a hot S-type thermocouple was imaged at different temperatures for calibration of the optical system. Subsequently, Eq. A.1 was used to create a look-up table relating the recorded colour ratio to the SiC temperature [22, 25].

The SiC filaments used here (Ceramics Grade Nicalon, COI Ceramics Inc.) were reported to be mechanically and optically stable while having a diameter of only 14 μm, making them ideal for TFP measurements [25]. It was reported that their emissivity can be assumed to be wavelength independent and that their optical properties remain constant for 60 min [25]. Consequently, the SiC filaments used in this study were replaced after each experiment or after 60 minutes at the latest.

During the experiments, the filament was placed over two metal rods (Fig. 6b). Small weights were mounted on each end of the filament to keep it in place and maintain a small tension to minimise curving and vibration of the filament induced by the flow. The filament was imaged with a Blackfly S (BFS-U3-32S4C-C, FLIR Integrated Imaging Solutions, Inc.) having a 1/1.8" Sony IMX252 CMOS sensor with 2048×1536 pixels (pixel size 3.45 µm). The camera lens was a MVL50M23 with an aperture set to f/2.0 and a focal length of 35 mm. The distance between the camera and the filament was 25 cm, resulting in a pixel width corresponding to 1/73 mm in the focal plane through the centre of the flame where the filament was positioned. A BG-7 filter (Thorlabs) was used to balance the intensity ratios of the three colour channels and to block infrared light. The filament was moved in steps of 0.1 mm in vertical direction through the flame using a manual translation stage (M-423, Newport) and a SM-25 Vernier Micrometer (Newport) with a 1.0 µm sensitivity and 10 µm graduations. At each step the camera exposure time was adjusted to maximise the signal from the SiC filament without saturating any of the three colour channels and 50 frames were recorded.

The images were analysed using an in-house developed Python code. The code searches for the SiC filament in the image and calculates its position. Note that due to the high flow velocities, the filament can be slightly curved. In case of high background light intensities (i.e., high camera exposure and emission from CH*), a spline was used to subtract the background from the SiC signal. The colour ratio at each horizontal pixel position is calculated and converted to the filament temperature, T_{SiC}.

Once the filament temperature T_{SiC} is known, it is corrected for radiative heat loss to obtain the gas temperature T_{g} [25]:

$$T_{\mathrm{g}} = \frac{\varepsilon\sigma(T_{\mathrm{SiC}}^4 - T_{\infty}^4)}{h} + T_{\mathrm{SiC}}, \tag{A.2}$$

where T_{∞} is the ambient temperature and h is the convective heat transfer coefficient given by:

$$h = \frac{\mathrm{Nu}\, k_{\mathrm{gas}}}{d_{\mathrm{SiC}}}. \tag{A.3}$$

Here, k_{gas} is the gas thermal conductivity and d_{SiC} is the filament diameter (14 μm in this case). A range of expressions are given in literature for the Nusselt number Nu depending flow conditions (natural or forced convection, Reynolds number Re) and object geometry (cylinder diameter and aspect ratio). An equation for forced convection over a cylinder perpendicular to the flow direction that was previously used for correcting SiC filament measurements is [25, 34]:

$$\mathrm{Nu}_{90} = a\mathrm{Re}^n. \tag{A.4}$$

The subscript 90 indicates the perpendicular flow direction. The constant a and n depend on the range of the Reynolds number, Re. In the present study, the following values were used: $a = 0.565$ and $n = 0.136$ when $0.03 \leq \mathrm{Re} \leq 0.09$ and $a = 0.800$ and $n = 0.280$ when $0.09 \leq \mathrm{Re} \leq 0.61$ [34].

The above expression is suitable in the flame centre line where the gas flow is truly perpendicular to the filament orientation. Away from the centre, the filament can be seen as an inclined or tilted cylinder heated by forced convection. In this study, the expression for Nu_{90} was corrected for the inclination angle Φ [30]:

$$\mathrm{Nu}_{\Phi} = \mathrm{Nu}_{90}(\sin^2\Phi + F^2\cos^2\Phi)^{0.5n_1} \tag{A.5}$$

Possible values for the constants F and n_1 are tabulated in [30, 44]. Values of $F = 0.2$ and $n_1 = 0.5$ were used here because they were reported for small diameter cylinders with high aspect ratios. The remaining parameters required for the temperature correction (Re, k_{gas}, Φ) were obtained from the 2D simulation.

The temperature profiles of each flame were measured three times. The spatial location of each measurement was determined from the imaged filament to assure temperatures at the same spatial positions were averaged.

B Simulation Details

B.1 Governing Equations

The governing equations for laminar reacting flow are partial differential equations in space and time, t, which describe the conservation of mass,

$$\frac{\partial \rho}{\partial t} + \nabla \cdot (\rho U) = 0; \tag{B.1}$$

momentum,

$$\frac{\partial \rho U}{\partial t} + \nabla \cdot (\rho UU) = -\nabla p - \mu \left(\nabla U + (\nabla U)^{\intercal}\right); \tag{B.2}$$

species,

$$\frac{\partial \rho Y_i}{\partial t} + \nabla \cdot (\rho U Y_i) + \nabla \cdot (\rho V_i^c Y_i) = \dot{\omega}_i; \tag{B.3}$$

and energy,

$$c_p \frac{\partial \rho T}{\partial t} + c_p \nabla \cdot (\rho U T) = \nabla \cdot (\lambda \nabla T) - \left(\rho \sum_{i=1}^{N} c_{p_i} Y_i V_i^c\right) \cdot \nabla T + \dot{\omega}_{\mathrm{T}} \tag{B.4}$$

where ρ is density, U is velocity, Y_i is the mass fraction of species i, T is temperature, p is pressure, V_i^c is the corrected diffusive velocity of species i, $\dot{\omega}_i$ is the rate of formation of species i, $\dot{\omega}_T$ is the enthalpy heat release, μ is mixture viscosity, λ is the mixture thermal conductivity, c_p is the mixture heat capacity.

To ensure consistency between the 1D and 2D simulations, the ideal gas law and the following physical models are used in both sets of simulations. The viscosity of each species is described by the Lennard-Jones parameters[8], where μ_i is viscosity of species i, W_i is molecular weight, k_B is the Boltzmann constant, σ_i is the Lennard-Jones collision diameter, and $\Omega^{(2,2)*}$ is the collision integral based on reduced temperature.

$$\mu_i = \frac{5}{16} \frac{(\pi W_i k_B T)^{1/2}}{\pi \sigma_i^2 \Omega^{(2,2)*}} \tag{B.5}$$

The mixture viscosity is defined by a semi-empirical formula by Wilke[45] that has been modified by Bird et al. [8]:

$$\mu = \sum_{i=1}^{N} \frac{X_i \mu_i}{\sum_{j=1}^{N} X_j \phi_{ij}} \tag{B.6}$$

$$\phi_{ij} = \frac{1}{\sqrt{8}} \left(1 + \frac{W_i}{W_j}\right)^{-\frac{1}{2}} \left(1 + \left(\frac{\mu_i}{\mu_j}\right)^{\frac{1}{2}} \left(\frac{W_j}{W_i}\right)^{\frac{1}{4}}\right)^2 \tag{B.7}$$

where X is mole fraction and ϕ_{ij} is a dimensionless binary mixing quantity between species i and j.

The thermal conductivities of individual species, λ_i, are composed of translational, rotational, and vibrational contributions which are functions of the species shape and properties[33]. The mixture thermal conductivity is given by [28]:

$$\lambda = \frac{1}{2}\left(\sum_{i=1}^{N} X_i\lambda_i + \left[\sum_{i=1}^{N} X_i/\lambda_i\right]^{-1}\right). \tag{B.8}$$

The heat capacities, enthalpy, and entropy are described using JANAF polynomials[16].

$$D_{i,j} = \frac{3}{16}\left(\frac{2N_A k_B^3 T^3}{\pi W_{ij}}\right)^{1/2} \frac{1}{p\sigma_{ij}^2 \Omega^{(1,1*)}} \tag{B.9}$$

$$D_i = \frac{1-Y_i}{\sum_{j\neq i}^{N} \frac{X_j}{D_{ij}}} \tag{B.10}$$

The mixture-averaged approach of Hirschfelder and Curtiss is used to get a single diffusion coefficient, D_i, for each species to be used in the transport equation. The binary diffusion coefficient, $D_{i,j}$, given below, is a function of temperature and pressure; the reduced molecular weight, W_{ij}; the reduced collision diameter, σ_{ij}; and a collision integral, $\Omega^{(1,1)*}$[17]. This approach is not inherently mass conserving, so a corrective velocity, V_c, is applied to each species to ensure mass is conserved. The final, corrected diffusion velocity, V_i^c, is the sum of the mass flux and the corrective velocity.

$$V_i^c = V_i + V_c, \quad V_i = -D_i\frac{\nabla X_i}{X_i}, \quad V_c = -\sum_{j}^{N} Y_j V_j \tag{B.11}$$

B.2 2D Mesh

Figure 7 shows an example mesh used for Flame 1.

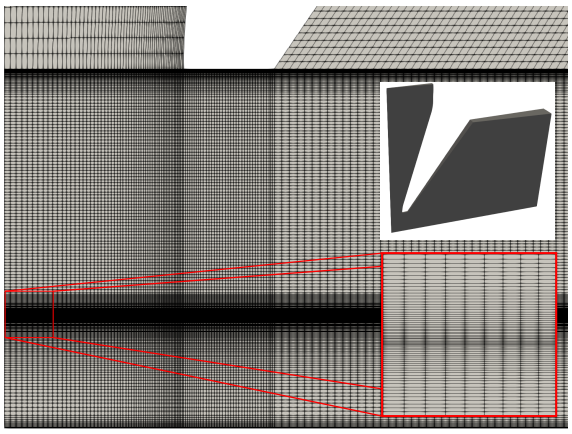

Figure 7: *Example Mesh for Flame 1. The inset figure, outlined in red, shows the refinement near the flame front.*

C Supporting Figures

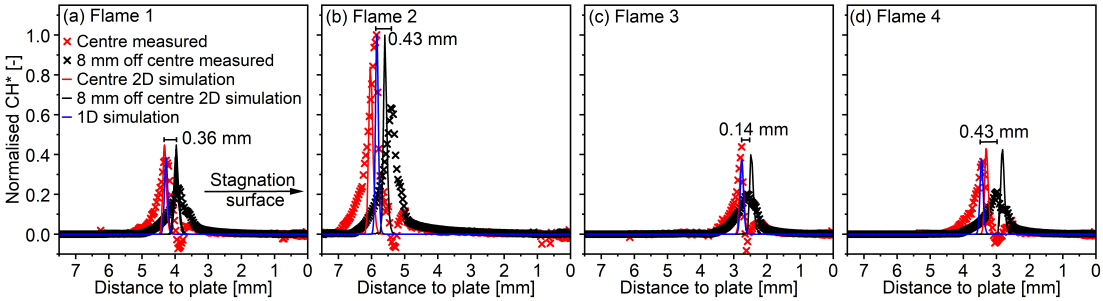

Figure 8: *Centre line and 8 mm off centre normalised CH* axial profiles with the addition of 1D simulation results.*

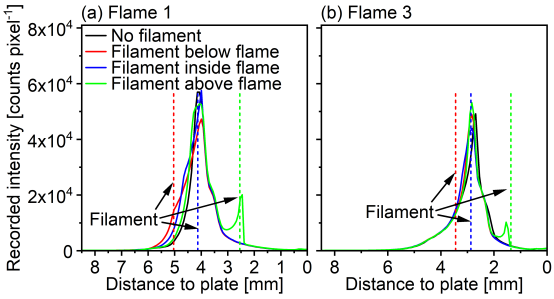

Figure 9: *Line profiles extracted from Fig. 3 of the main manuscript to highlight how the presence of the SiC filament influences the flames.*

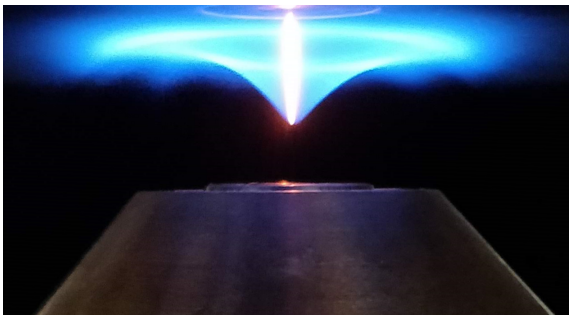

Figure 10: *Photograph of the flame disturbance when placing the SiC filament vertically into the flame.*

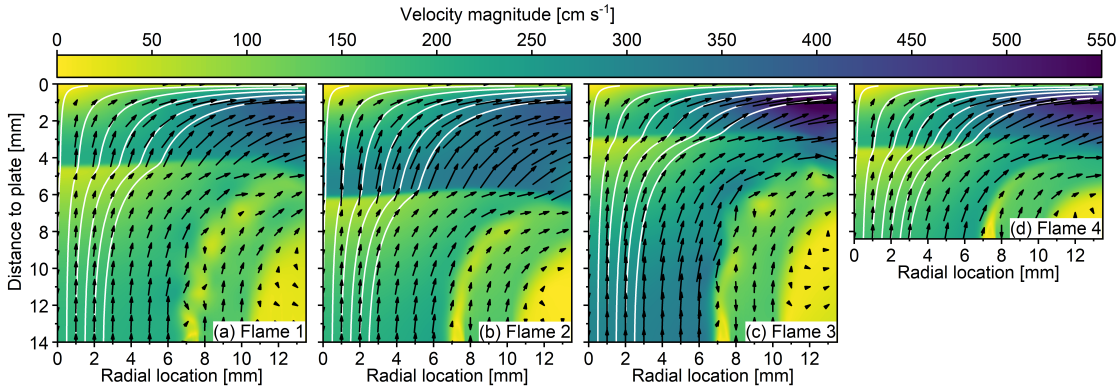

Figure 11: *Simulated 2D velocity fields of the four flames studied. Details regarding the flame parameters can be found in Table 1 of the main manuscript. The abrupt change in the streamlines occurs at the flame front.*

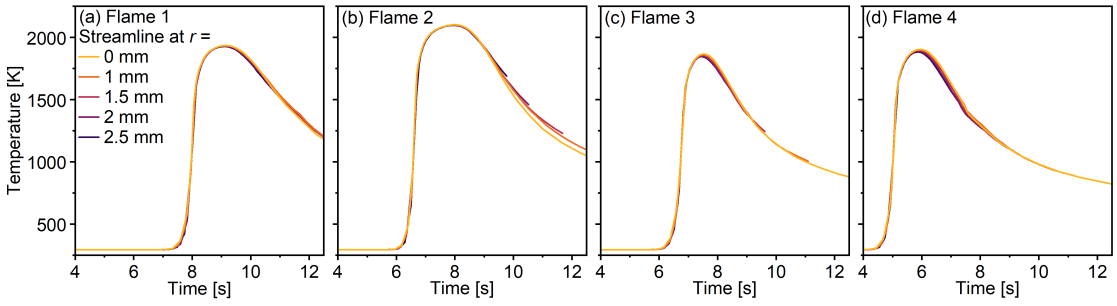

Figure 12: *Time-temperature profiles of the streamlines shown in Fig. 11. Except for the streamline at r = 0 mm, the curves were shifted on the abscissa such that the time at which they reach 1500 K is identical to the streamline at r = 0 mm.*

References

[1] A. Ansari and F. N. Egolfopoulos. Flame ignition in the counterflow configuration: Reassessing the experimental assumptions. *Combust. Flame*, 174:37 – 49, 2016. doi:10.1016/j.combustflame.2016.09.021.

[2] M. Apostolopoulos, M. Taroudakis, and D. Papazoglou. Application of inverse abel techniques in in-line holographic microscopy. *Opt. Commun.*, 296:25 – 34, 2013. doi:10.1016/j.optcom.2013.01.053.

[3] L. Benezech. Premixed hydrocarbon stagnation flames: Experiments and simulations to validate combustion chemical-kinetic models, June 2008.

[4] J. M. Bergthorson and P. E. Dimotakis. Premixed laminar C1-C2 stagnation flames: Experiments and simulations with detailed thermochemistry models. *Proc. Combust. Inst.*, 31(1):1139 – 1147, 2007. doi:10.1016/j.proci.2006.07.110.

[5] J. M. Bergthorson, K. Sone, T. W. Mattner, P. E. Dimotakis, D. G. Goodwin, and D. I. Meiron. Impinging laminar jets at moderate Reynolds numbers and separation distances. *Phys. Rev. E*, 72:066307, 2005. doi:10.1103/PhysRevE.72.066307.

[6] J. M. Bergthorson, S. D. Salusbury, and P. E. Dimotakis. Experiments and modelling of premixed laminar stagnation flame hydrodynamics. *J. Fluid Mech.*, 681:340–369, 2011. doi:10.1017/jfm.2011.203.

[7] J. M. Bergthrson. *Experiments and modeling of impinging jets and premixed hydrocarbon stagnation flames*. PhD thesis, California Institute of Technology, Pasadena, CA, May 2005.

[8] R. B. Bird, W. E. Stewart, and E. N. Lightfoot. *Transport Phenomena*. John Wiley & Sons, 2nd edition, 2001.

[9] N. Bouvet, D. Davidenko, C. Chauveau, L. Pillier, and Y. Yoon. On the simulation of laminar strained flames in stagnation flows: 1D and 2D approaches versus experiments. *Combust. Flame*, 161(2):438 – 452, 2014. doi:10.1016/j.combustflame.2013.09.010.

[10] CMCL Innovations. *k*inetics®, 2016.

[11] J. Dreyer, M. Poli, N. Eaves, M. Botero, J. Akroyd, S. Mosbach, and M. Kraft. Evolution of the soot particle size distribution along the centreline of an n-heptane/toluene co-flow diffusion flame. *Combust. Flame*, 209:256–266, 2019. doi:10.1016/j.combustflame.2019.08.002.

[12] J. A. H. Dreyer, R. I. Slavchov, E. J. Rees, J. Akroyd, M. Salamanca, S. Mosbach, and M. Kraft. Improved methodology for performing the inverse abel transform of flame images for color ratio pyrometry. *Appl. Opt.*, 58(10):2662–2670, Apr 2019. doi:10.1364/AO.58.002662.

[13] V. Dribinski, A. Ossadtchi, V. A. Mandelshtam, and H. Reisler. Reconstruction of Abel-transformable images: The Gaussian basis-set expansion Abel transform method. *Rev. Sci. Instrum.*, 73(7):2634–2642, 2002. doi:10.1063/1.1482156.

[14] F. Egolfopoulos, H. Zhang, and Z. Zhang. Wall effects on the propagation and extinction of steady, strained, laminar premixed flames. *Combust. Flame*, 109(1-2): 237–252, 1997. doi:10.1016/S0010-2180(96)00152-6.

[15] C. Frouzakis, J. Lee, A. Tomboulides, and K. Boulouchos. Two-dimensional direct numerical simulation of opposed-jet hydrogen-air diffusion flame. *Proc. Combust. Inst.*, 27(1):571 – 577, 1998. doi:10.1016/S0082-0784(98)80448-7.

[16] S. Gordon and B. J. McBride. Computer program for calculation of complex chemical equilibrium compositions, rocket performance, incident and reflected shocks and chapman-jouguet detonations. Technical Report NASA Report SP-273, National Aeronautics and Space Administration, Washington, DC, United States, March 1976. URL https://ntrs.nasa.gov/archive/nasa/casi.ntrs.nasa.gov/19780009781.pdf.

[17] J. O. Hirschfelder, C. F. Curtiss, and R. B. Bird. *Transport Phenomena*. John Wiley & Sons, 2nd edition, 1954.

[18] R. Issa. Solution of the implicitly discretised fluid flow equations by operator-splitting. *J. Comput. Phys.*, 62(1):40 – 65, 1986. doi:10.1016/0021-9991(86)90099-9.

[19] R. Johnson, A. VanDine, G. Esposito, and H. Chelliah. On the axisymmetric counterflow flame simulations: is there an optimal nozzle diameter and separation distance to apply quasi one-dimensional theory? *Combust. Sci. Technol.*, 187(1-2):37–59, 2015. doi:10.1080/00102202.2014.972503.

[20] R. J. Kee, J. A. Miller, G. H. Evans, and G. Dixon-Lewis. A computational model of the structure and extinction of strained, opposed flow, premixed methane-air flames. *Proc. Combust. Inst.*, 22(1):1479 – 1494, 1989. doi:10.1016/S0082-0784(89)80158-4.

[21] A. A. Konnov, A. Mohammad, V. R. Kishore, N. I. Kim, C. Prathap, and S. Kumar. A comprehensive review of measurements and data analysis of laminar burning velocities for various fuel+air mixtures. *Prog. Energy Combust. Sci.*, 68:197 – 267, 2018. doi:10.1016/j.pecs.2018.05.003.

[22] P. B. Kuhn, B. Ma, B. C. Connelly, M. D. Smooke, and M. B. Long. Soot and thin-filament pyrometry using a color digital camera. *Proc. Combust. Inst.*, 33(1):743 – 750, 2011. doi:10.1016/j.proci.2010.05.006.

[23] C. S. Lindberg, M. Y. Manuputty, P. Buerger, J. Akroyd, and M. Kraft. Numerical simulation and parametric sensitivity study of titanium dioxide particles synthesised in a stagnation flame. *J. Aerosol Sci.*, 138:105451, 2019. doi:10.1016/j.jaerosci.2019.105451.

[24] B. Ma and M. B. Long. Absolute light calibration using S-type thermocouples. *Proc. Combust. Inst.*, 34(2):3531 – 3539, 2013. doi:10.1016/j.proci.2012.05.030.

[25] B. Ma, G. Wang, G. Magnotti, R. S. Barlow, and M. B. Long. Intensity-ratio and color-ratio thin-filament pyrometry: Uncertainties and accuracy. *Combust. Flame*, 161(4):908 – 916, 2014. doi:10.1016/j.combustflame.2013.10.014.

[26] M. Manuputty, J. Dreyer, Y. Sheng, E. Bringley, M. Botero, J. Akroyd, and M. Kraft. Polymorphism of nanocrystalline TiO_2 prepared in a stagnation flame: formation of the TiO_2-II phase. *Chem. Sci.*, 10:1342–1350, 2019. doi:10.1016/j.combustflame.2006.12.001.

[27] M. Y. Manuputty, J. Akroyd, S. Mosbach, and M. Kraft. Modelling TiO_2 formation in a stagnation flame using method of moments with interpolative closure. *Combust. Flame*, 178:135 – 147, 2017. doi:10.1016/j.combustflame.2017.01.005.

[28] S. Mathur, P. Tondon, and S. Saxena. Thermal conductivity of binary, ternary and quaternary mixtures of rare gases. *Mol. Phys.*, 12(6):569–579, 1967. doi:10.1080/00268976700100731.

[29] V. Mittal, H. Pitsch, and F. Egolfopoulos. Assessment of counterflow to measure laminar burning velocities using direct numerical simulations. *Combust. Theory Model.*, 16(3):419–433, 2012. doi:10.1080/13647830.2011.631033.

[30] V. T. Morgan. The overall convective heat transfer from smooth circular cylinders. *Adv. Heat Transf.*, 11:199 – 264, 1975. doi:10.1016/S0065-2717(08)70075-3.

[31] V. N. Nori. *Modeling and Analysis of Chemiluminescence sensing for syngas, methane, and Jet-A Combustion*. PhD thesis, Georgia Institute of Technology, Atlanta, GA, August 2008.

[32] C. B. Oh, A. Hamins, M. Bundy, and J. Park. The two-dimensional structure of low strain rate counterflow nonpremixed-methane flames in normal and microgravity. *Combust. Theory Model.*, 12(2):283–302, 2008. doi:10.1080/13647830701642201.

[33] N. Peters and J. Warnatz, editors. *Discussion of Test Problem B*, chapter J. Warnatz, pages 49–64. Vieweg+Teubner Verlag, Wiesbaden, 198. doi:10.1007/978-3-663-14006-1_5.

[34] W. M. Rohsenow, J. P. Hartnett, Y. I. Cho, et al. *Handbook of Heat Transfer*. McGraw-Hill, 3 edition, 1998.

[35] M. Smooke, C. McEnally, L. Pfefferle, R. Hall, and M. Colket. Computational and experimental study of soot formation in a coflow, laminar diffusion flame. *Combust. Flame*, 117(1):117 – 139, 1999. doi:10.1016/S0010-2180(98)00096-0.

[36] K. Sone. *Modeling and simulation of axisymmetric stagnation flames*. PhD thesis, California Institute of Technology, Pasadena, CA, May 2007.

[37] The OpenFOAM Foundation Ltd. Openfoam v5.x, 2016.

[38] E. D. Tolmachoff, A. D. Abid, D. J. Phares, C. S. Campbell, and H. Wang. Synthesis of nano-phase TiO_2 crystalline films over premixed stagnation flames. *Proc. Combust. Inst.*, 32(2):1839 – 1845, 2009. doi:10.1016/j.proci.2008.06.052.

[39] C. M. Vagelopoulos and F. N. Egolfopoulos. Direct experimental determination of laminar flame speeds. *Proc. Combust. Inst.*, 27(1):513 – 519, 1998. doi:10.1016/S0082-0784(98)80441-4.

[40] P. Versailles, G. M. G. Watson, A. Durocher, G. Bourque, and J. M. Bergthorson. Thermochemical Mechanism Optimization for Accurate Predictions of CH Concentrations in Premixed Flames of C1-C3 Alkane Fuels. *J. Eng. Gas Turb Power*, 140 (6), 2018. doi:10.1115/1.4038416.

[41] K. Wang, F. Li, Y. Wu, and X. Yu. Quantitative measurements of chemiluminescence in a laminar methane-air premixed flame and comparison to numerical methods. *Energy Fuels*, 32(4):5536–5543, 2018. doi:10.1021/acs.energyfuels.7b03484.

[42] G. M. Watson, P. Versailles, and J. M. Bergthorson. NO formation in premixed flames of C1-C3 alkanes and alcohols. *Combust. Flame*, 169:242 – 260, 2016. doi:https://doi.org/10.1016/j.combustflame.2016.04.015.

[43] G. M. Watson, P. Versailles, and J. M. Bergthorson. NO formation in rich premixed flames of C1-C4 alkanes and alcohols. *Proc. Combust. Inst.*, 36(1):627 – 635, 2017. doi:10.1016/j.proci.2016.06.108.

[44] C. A. G. Webster. A note on the sensitivity to yaw of a hot-wire anemometer. *J. Fluid Mech.*, 13(2):307–312, 1962. doi:10.1017/S0022112062000695.

[45] C. Wilke. A viscosity equation for gas mixtures. *J. Chem. Phys.*, 18(4):517–519, 1950. doi:10.1063/1.1747673.

[46] F. Williams et al. Chemical-kinetic mechanisms for combustion applications. San Diego Mechanism web page, Mechanical and Aerospace Engineering (Combustion Research), University of California at San Diego http://combustion.ucsd.edu/ (2005).